Supporting Information

Gharib et al. 10.1073/pnas.1712717114

SI Detailed Calculations

Electron Density. We define the current density as $j = n_e \cdot e \cdot v_d = E/\eta$, where n_e is the electron density, e the elementary charge, v_d the electron mean drift velocity, E the electric strength, and η the plasma resistivity. We have $\eta = m_e\,(\nu_{ei} + \nu_{en})/n_e\,e^2$, where m_e is the electron mass and ν_{ei} and ν_{en} are the electron–ion and electron–neutral collisional rates, respectively. Assuming electron–electron collisions are negligible, the momentum balance equation results in $\nu_{ei} = e\,E/m_e\,v_d - \nu_{en}$ at steady state.

The electron–neutral collision rate is $\nu_{en} = \sigma_e n_n v_{Te}$, where σ_e is the electron–neutral collisional cross-section, n_n the density of neutral gas particles, and v_{T_e} the electron thermal velocity defined (24) as $v_{T_e} = \sqrt{T_e/m_e} \approx 6.81 \times 10^7$ cm$\cdot$s^{-1} for $T_e = 2.64$ eV. Using the average atomic radius of the two main constituents of air (nitrogen and oxygen), the collision cross-sectional area σ_e is 3.4×10^{-16} cm^2. Finally, the electron drift velocity v_d is a function of the reduced field strength E/n_n (25). For the values measured with the air plasma, the mean electron drift velocity v_d is 3.06×10^7 cm$\cdot$s^{-1}.

The Spitzer resistivity associated with electron–ion collisions is given (48) by $\eta_s = Z\,e^2\,\sqrt{m_e}\,4\sqrt{2\pi}\,\ln\Lambda/3\,(4\pi\epsilon_0)^2\,T_e^{3/2}$,where Z is the charge state, ϵ_0 the free space permittivity, and T_e the electron temperature in eV. $\ln\Lambda$ is the Coulomb logarithm, which is defined (24) as $\ln\Lambda = 23 - \ln(n_e^{1/2}/T_e^{3/2})$ for $T_e < 10$ eV. By substituting the term $m_e\nu_{ei}/n_e e^2$ in the definition of the total resistivity η by the Spitzer resistivity η_s, n_e can be determined for $T_e = 2.64$ eV and $Z = 1$, for we assume singly ionized air molecules in our calculations. We find $\ln\Lambda = 4.64$, a plasma resistivity $\eta = 12.6 \times 10^{-5}\ \Omega\cdot$m, and an electron density $n_e = 1.62 \times 10^{17}$ cm^{-3}. Electron pressure is 6.84×10^4 Pa. Ultimately the current density is $j = 7.93$ mA$\cdot\mu$m^{-2}, corresponding to a dissipated power $j \cdot E \cdot V_p \approx 80$ W based on a plasma volume $V_p \sim 10^{-14}$ m^3 (Fig. 1*B*). To validate this estimate, we note that the power dissipated by a jet with diameter 85 μm flowing at 350 m$\cdot$s^{-1} and impacting on a wall is ∼120 W, assuming total dissipation on impact.

Plasma Oscillations. Plasma frequencies are given by the Tonks–Langmuir relations (24) $\omega_{pe} = \sqrt{n_e\,e^2/m_e\,\epsilon_0}$ and $\omega_{pi} = \sqrt{n_i\,(Ze)^2/m_i\,\epsilon_0}$, respectively the plasma–electron and the plasma–ion frequencies, with n_i being the ion density and $m_i = A \cdot m_p$ the ion mass, where A is the atomic number and m_p the proton mass. Assuming singly ionized N_2 molecules such that $Z = 1$ and $A = 14$, and under the assumption of quasi-neutrality implying $n_i \sim n_e$, we obtain $\omega_{pi} = \omega_{pe}\sqrt{m_e/m_i}$. The ion field oscillates at a much lower frequency than the electron field as a consequence of the ∼25,000 mass ratio between N_2^+ and the electron. For $n_e = 1.62 \times 10^{17}$ cm^{-3}, we obtain $\omega_{pe}/2\pi = 3.61$ THz and $\omega_{pi}/2\pi = 22.5$ GHz.

Ion Acoustic Waves. In its simplest form, the dispersion relation for the ion acoustic wave is (29, 48) $\omega = k\,c_s/\sqrt{1 + k^2\lambda_{De}^2}$, where k is the wavenumber, c_s is the ion acoustic velocity given by $c_s = \omega_{pi}\lambda_{De} = \sqrt{T_e/m_i}$ (24), and λ_{De} is the Debye length defined as $\lambda_{De} = \sqrt{\epsilon_0\,T_e/n_e\,e^2}$ (24), T_e being expressed in eV. We obtain $\lambda_{De} \simeq 30$ nm and $c_s \simeq 4.25 \times 10^5$ cm$\cdot$s^{-1}.

If $k^2\lambda_{De}^2 \gg 1$, ω saturates as expected at $c_s/\lambda_{De} = \omega_{pi}$, the plasma–ion frequency. If we now assume that $k^2\lambda_{De}^2 \ll 1$, the wavenumber matching the 36-MHz peak is $k = \omega/c_s \approx 5.32 \times 10^4$ rad$\cdot$m^{-1}, leading to $k^2\lambda_{De}^2 \approx 2.55 \times 10^{-6}$, which validates the initial assumption. Furthermore, the onset of ion acoustic instabilities occurs when $\omega_{pi}\,v_d/\nu_{in}\,v_{T_e} \geq \sqrt{27/2\pi}$ (29), where $\nu_{in} = \sigma_i n_n v_{T_i}$ is the ion–neutral collision frequency, with $\sigma_i = 1.47 \times 10^{-15}$ cm^2 being the ion–neutral collisional cross-section and v_{T_i} the ion thermal velocity defined as $v_{T_i} = \sqrt{T_i/m_i}$ (24). Taking T_i as equal to the mean gas temperature $T_g = 1{,}250$ K≈ 0.11 eV, we obtain $v_{T_i} = 8.6 \times 10^4$ cm$\cdot$s^{-1}. Hence the ion–neutral collision frequency is $\nu_{in} = 3.6 \times 10^8$ s^{-1} and $\omega_{pi}\,v_d/\nu_{in}\,v_{T_e} \sim 178$. The condition for the onset of ion acoustic instabilities is therefore also satisfied.

Water pH. In the air gas phase (Table S1 *A–H*), N_2 and O_2 split through electron collisions with bond-dissociating energies of 941 kJ$\cdot$mol^{-1} and 498 kJ$\cdot$mol^{-1}, respectively. The highly reactive nitrogen atoms recombine into N_2^+ ions and free electrons through associative ionization. Combination with O_2 atoms and the Zeldovich reactions leads to nitric oxide $^\bullet$NO (Table S1 *C* and *D*), which bonds with oxygen to form nitrogen dioxide $^\bullet NO_2$. Highly soluble in water, $^\bullet NO_2$ hydrolyses with H_2O molecules at the air–water interface to produce nitrous acid HNO_2 and nitric acid HNO_3. In aqueous solution and because of the polar nature of water, these acids split into hydrons H^+ and the respective conjugate bases NO_2^- (nitrite) and NO_3^- (nitrate). Hydrogen ions H^+ bond with H_2O to form the hydronium ion H_3O^+, the conjugate acid of water.

In absence of plasma, nitrite-N in water sampled at the wafer edge (*SI Materials and Methods*) was not detected whereas nitrate-N levels averaged to 0.09 ppm. When the air corona was active, nitrite-N and nitrate-N levels averaged 0.025 ppm and 0.15 ppm, respectively, corresponding to a nitrite concentration of 1.78×10^{-6} mol/L and to an effective nitrate concentration of 2.49×10^{-6} mol/L. The corresponding concentration of cations H^+/H_3O^+ added to the water is 4.28×10^{-6} mol/L, causing the pH to drop from 5.6 to 5.17.

Solvated Electrons. The positive ions produced in air are accelerated by the electric field, bombarding H_2O molecules at the air–water interface to produce (Table S1 *I–O*) excited water molecules H_2O^*, H_2O^+ cations, and hydrated electrons $e_{(aq)}$ (49). Short-lived in water (50, 51) and confined within nanometers from the surface (34), these solvated electrons are released into the gas phase through a chemical tunneling effect (33) (Table S1 *L–O*). This secondary pathway to electron emission needs only 1.56 eV (26). A low pH promotes the protonation of water and the reaction rate between H_3O^+ and the hydrated electrons, enhancing the electron release (52).

Energy Balance. In air, dissociation of O_2 (9.75 eV) and N_2 (5.16 eV), excitation and ionization of air molecules (>2.64 eV), and secondary electron emission (1.56 eV) amount to ∼19.1 eV. With helium, H_2O dissociation (5.11 eV), excitation and ionization of OH (>4 eV) and H (>10.2 eV), and excitation of He atoms (>3.37 eV) amount to ∼22.7 eV.

SI Materials and Methods

General Information. The experimental pump setup is based on a DSF-model Haskell fluid pump driven by building air pressure. The air pressure delivered to the system was kept below 159 PSI, resulting in a maximal liquid output pressure of 16,500 PSI and a corresponding jet speed of 430 m$\cdot$s^{-1}. A water reservoir delivers a constant, deionized water supply through the pump to an AccuStream waterjet system equipped with a 100-μm diameter

ruby nozzle. The jet contracts due to the vena cava effect to a diameter of 85 μm and keeps this value until the point of impingement. The distance between the nozzle tip and the surface was kept at 20 mm to avoid jet breakup and spray formation. The water delivered to the system was refreshed at least once daily to keep ion concentration low in the system. Water pH was measured with a Spectrum Technologies IQ 150 pH meter and water resistivity was measured with a Fluke 287 multimeter with dual brass probes.

Target wafers tested were methyl acrylate, niobium, lithium niobate (X-cut, Y-cut, Z-cut, polished, and fine ground), fused quartz, seeded quartz (polished and fine ground), borosilicate glass, silicon, and sapphire (polished and fine ground). Around the target wafers, a hermetic acrylic container was designed that allowed gas input for gas exchange, a positive pressure drain for water and air purging, and a cutout beneath the wafer stage, which allowed optical access through the wafers to the impinging jet site.

A Nikon D90 or a Sony A7S digital camera was adapted to fixed-focus microscope objectives for imaging through the optical cutout, with constant settings and neutral white balance used for all images unless otherwise noted. A Quest *U* BRC112P-U CCD array spectrometer (B&W Tek, Inc.) was used to record optical spectra in the range of 300–850 nm through the same optics and was equipped with a 10-μm slit giving a spectral resolution of 0.3–0.4 nm. RF as well as electric field measurements were done digitally with a Tektronix MDO3024 mixed-domain oscilloscope.

Calibration of Jet Velocity. The digitally measured jet diameter at the impingement distance in combination with the average liquid flow rate through the jet nozzle allowed the back calculation of the average velocity of the jet at a range of input pump pressures. To measure the flow output, the jet was turned on for 30 s while the output water was captured in a graduated cylinder. Input pressures from 30 PSI up to 150 PSI were tested, resulting in an output volume ranging from 27.2 ml to 75.2 ml during this period of 30 s. Given a jet diameter of 85 μm, a quadratic regression of the measurements provided the following approximation for the jet velocity U,

$$U(P) = -0.0255\,P^2 + 6.29595\,P - 3.07143 \qquad (R^2 = 0.998),$$

where U is given in $\mathrm{m \cdot s^{-1}}$ and P is the pump pressure given in PSI. The maximum tenable average jet velocity was $428\ \mathrm{m \cdot s^{-1}}$.

Target Materials. We observed a variety of behaviors from the dielectric materials tested. Methyl acrylate was quickly damaged by the jet, yet did generate luminescence. Borosilicate glass generated luminescence and cracked after several minutes, releasing glass shards. Niobium and silicon wafers were durable but failed to generate any luminescence. Quartz, lithium niobate, and sapphire samples generated luminescence and were hard enough to withstand the pressure of the impinging jet. Of these latter materials, single crystal quartz (SiO_2) and single crystal lithium niobate (Z-cut $LiNbO_3$) required significantly lower activation water pressures than did sapphire. With an optical transmittance higher than 50% up from wavelengths of ∼150 nm for SiO_2 and ∼320 nm for $LiNbO_3$, these materials were also suitable for optical and spectral analysis. Surface quality was either polished (microroughness $Ra < 10$ Å) or fine ground (microroughness $Ra < 1$ μm).

Water Resistivity. Water resistivity in the reservoir measured an average of $18\ \mathrm{M\Omega \cdot cm}$. Failure to refresh water stores for a period of 18 h resulted in a drop in resistivity from $18\ \mathrm{M\Omega \cdot cm}$ to $4.5\ \mathrm{M\Omega \cdot cm}$. At $4.5\ \mathrm{M\Omega \cdot cm}$, the corona was not stable, intermittent, or at times absent.

Measurement of pH. To assess any pH change in the deionized water that was exclusively a result of the luminescent process itself, water was collected into a glass reservoir following jet impingement in the presence and in the absence of a corona. The pH meter was calibrated with stock buffer solutions. Source water pH was measured to be 7.1 on average. Running the water through the pump tubing lowered the pH to 5.6 ± 0.03 at the nozzle.

Physico-Chemical Characterization of Water. We tested the presence of nitrites and nitrates in the water upstream and downstream of the impinging site, in absence and presence of air corona and when the gas was changed from air to helium. The water was sampled at the jet outlet before impingement and at the edge of the wafer plate after impingement.

Nitrite levels were measured with a nitrite–nitrogen ($NO_2^- - N$) Ultra Low Range HI764 photometer test kit from Hanna Instruments. The $NO_2^- - N$ detection method uses an adaptation of the EPA diazotization method 354.1. The effective range of the photometer kit is from 0 ppb to 200 ppb $NO_2^- - N$ ± 10 ppb ± 4% of reading at 25 °C. Resolution is 1 ppb.

Nitrate levels were measured with a low-range nitrate–nitrogen ($NO_3^- - N$) photometer test kit from Environmental Express. The $NO_3^- - N$ detection method uses eukaryotic nitrate reductase to convert available nitrates into nitrites, followed by the same diazotization method used to measure nitrite–nitrogen levels. The effective range of the photometer kit is from 0.05 ppm to 2.0 ppm $NO_3^- - N$ ± 10%. Total measured $NO_2^- - N$ results from both actual $NO_2^- - N$ and converted $NO_3^- - N$. Therefore, the actual content of nitrates is calculated using the separate measurement of the concentration of nitrites alone with the nitrite–nitrogen kit.

Imaging. Although light emitted by the luminescent phenomenon was detectable without magnification, viewing the corona through the optical cutout with high magnifications revealed important topological features. Fig. 1*B* was taken at ISO 640 with a 1/5-s exposure time, using a Nikon D90 camera mounted on a 160-mm–long microscope tube coupled with a 50× objective lens. Using a Sony A7S camera with a 1/60-s exposure time and a 10× objective lens, photographs in Fig. 1*C* and Figs. S1 and S3 were captured at ISO 20,000, whereas photographs in Fig. 2*A* and Figs. S4 and S5 were taken at ISO 12,800.

Optical Emission Spectroscopy. To calibrate the sensitivity of the B&W Tek, Inc. spectrometer across as much of its range as possible, optical spectra of an Oriel sun simulator (LCS-100 Solar Simulator, model 91104A) were recorded without magnification. True spectral data of the same Oriel sun simulator were provided by the manufacturer, which were then compared with the readout of our spectrometer. A built-in calibration function adjusted values accordingly.

In the experimental setup, the optical fiber from the spectrometer was connected to a full-pass collimator with C-mount threading. This adapter allowed the Nikon D90/Sony A7S cameras and the spectrometer collimator to be interchanged, using the same objective lens without moving it. Connecting both devices to the same objective allowed all light passed to the camera sensor to also pass to the spectrometer CCD. The focal tube connected to the microscope objectives was mounted beneath the acrylic container and the target wafer.

Before each spectroscopy session, all sources of ambient light were shut off to ensure sterility in the readings. A background signal was recorded and stored each time. For both background and signal spectra recordings, the integration time was set to 200 ms with 15 time averages and a multiplier of 10 for a total recording time of 30 s. Dark subtraction and intensity calibration were also implemented for all spectra.

RF Measurements. Using the spectrum analyzer function of the Tektronix digital oscilloscope, RF emissions of the luminescent phenomenon were recorded between 1 MHz and 100 MHz for lithium niobate and seeded quartz wafers. Twenty-two–gauge enamel-coated wire was wound around an acrylic cylinder 10 mm in diameter and glued with thermoplastic adhesive to maintain its shape. The acrylic core was then removed to leave the structure forming the antenna as shown in Fig. S6.

RF emissions were recorded and averaged over 512 samples ($\sim$15 s) with the antenna firm in its measuring position. Before jet initialization, background emissions were also recorded.

Electrical Grounding of Wafer. A brass needle was positioned underneath the wafer on a three-axis microtraverse system, which allowed one to press the needle against the plate and move it radially away from the point of impingement on the reverse side of the wafer. The bent tip of the needle allowed some force to be applied to the needle to ensure contact. The opposite end of the needle was then connected to an electrical ground.

Electric Field Mapping. Probing the interior of a plasma is usually done by sweeping the voltage on the probe and measuring the resultant probe current. Our analysis, however, was not for the interior of the plasma but for the electric field emitted by it. Measuring equipotential surfaces and mapping electric field lines are commonly done with a probe at a fixed potential paired with a floating probe which measures the potential at various points in the electric field. The potential of the interior of the plasma was determined to be consistent enough to act as a reference potential. The electric field exterior to the plasma was then measured with a free probe at various points throughout the field.

Mapping the electric field via voltage measurements was done using the digital voltmeter function on the Tektronix oscilloscope. Two brass needles were encased with a two-coat hydrophobic and electrically insulating layer. The tips were then cleaned of this layer to expose a small conductive area. Each needle was then connected to different three-axis microtraverses. The reference probe tip was positioned within 75 μm of the jet boundary. When the probe tip was moved closer, the position of the probe interfered with the jet structure. The other probe tip was initially positioned adjacent to the reference probe and then moved incrementally outward along the horizontal and vertical axes, independently. Voltage measurements were recorded and averaged for 30 s at each point. A contour map of the averaged values of voltages around the site of impingement is shown in Fig. 3.

The probes were set up such that the positive voltmeter terminal remained near the jet annulus as the reference electrode. In this configuration all measured values were negative, indicating a surplus of negative charge carriers (electrons) around the jet annulus compared with the charges in the air at distances away from the corona. To determine the electric field lines, the sparse data of the potential field were interpolated using Hermite polynomials and spatially derived between all data points, resulting in the white arrowed lines shown in Fig. 3. In Fig. 3, extrapolated data are reported as dashed black lines in the region between 75 μm and the jet boundary.

Jet Flow Simulations. The water jet of diameter 85 μm impinged vertically on a solid wall with a velocity of 250 $m \cdot s^{-1}$, corresponding to a Reynolds number of 21,250 based on the jet diameter. The domain of computation was 240 μm × 1,000 μm in the axial and radial directions, respectively. Zero velocity was imposed at the wall and zero-gauge pressure was specified at the outer boundaries.

The 2D, laminar, incompressible, axisymmetric, unsteady two-phase flow Navier–Stokes equations were solved until steady state was reached. The implicit volume-of-fluid method together with the compressive interface-capturing scheme for arbitrary meshes was used to model the sharp interface between the water jet and the surrounding air. The Ansys Fluent 16.0 CFD package was used to solve the discrete problem. The second-order upwind spatial scheme with the PRESTO! pressure approximation was used. Following a mesh-independence test, the 2D quadrilateral mesh consisted of 180,000 nodes with four-level mesh adaptation in the vicinity of the wall and of the free surface. The node spacing near the wall and the free surface was below 0.013 μm and 0.2 μm, respectively.

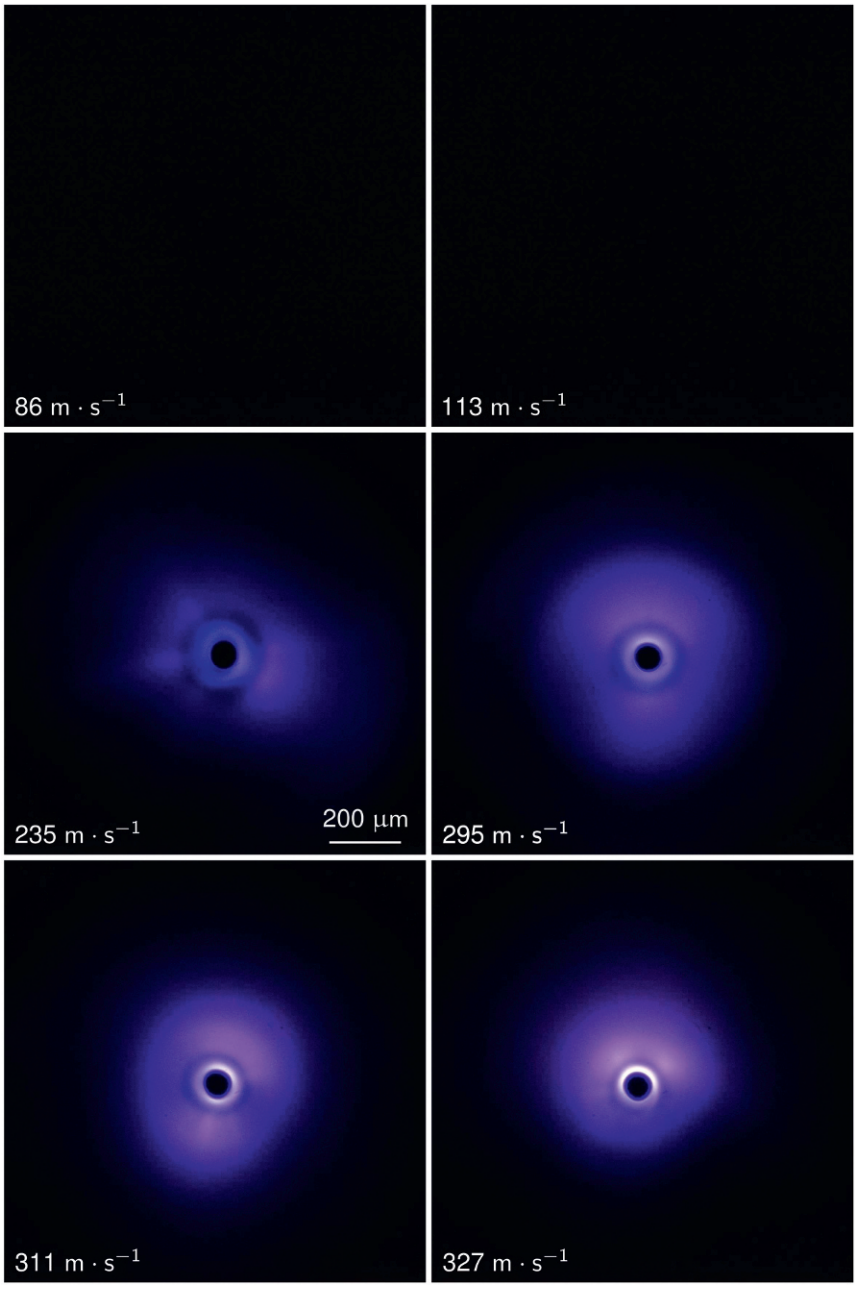

Fig. S1. Luminescence in air on a polished quartz surface. Jet velocity is varied from 86 m · s^{-1} to 327 m · s^{-1}. Photographs were taken at ISO 20,000 and a 1/60-s exposure time with a Sony A7S camera and a 10× objective lens. Color levels of images have been enhanced by 33% for better display.

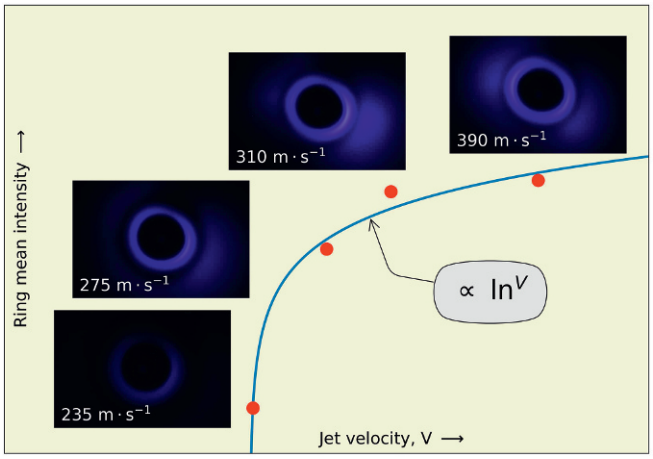

Fig. S2. Increase in corona luminosity with increase in impingement velocity. As the water pressure rises, the outlet velocity increases and a corresponding monotonic increase in light intensity follows. The luminescent patterns were observed on a polished quartz wafer. We noted that the intensity of the luminescent ring increased logarithmically with the velocity. Photographs were taken at ISO 1,000 and a 1/5-s exposure time with a Nikon D90 camera and a 50× objective lens.

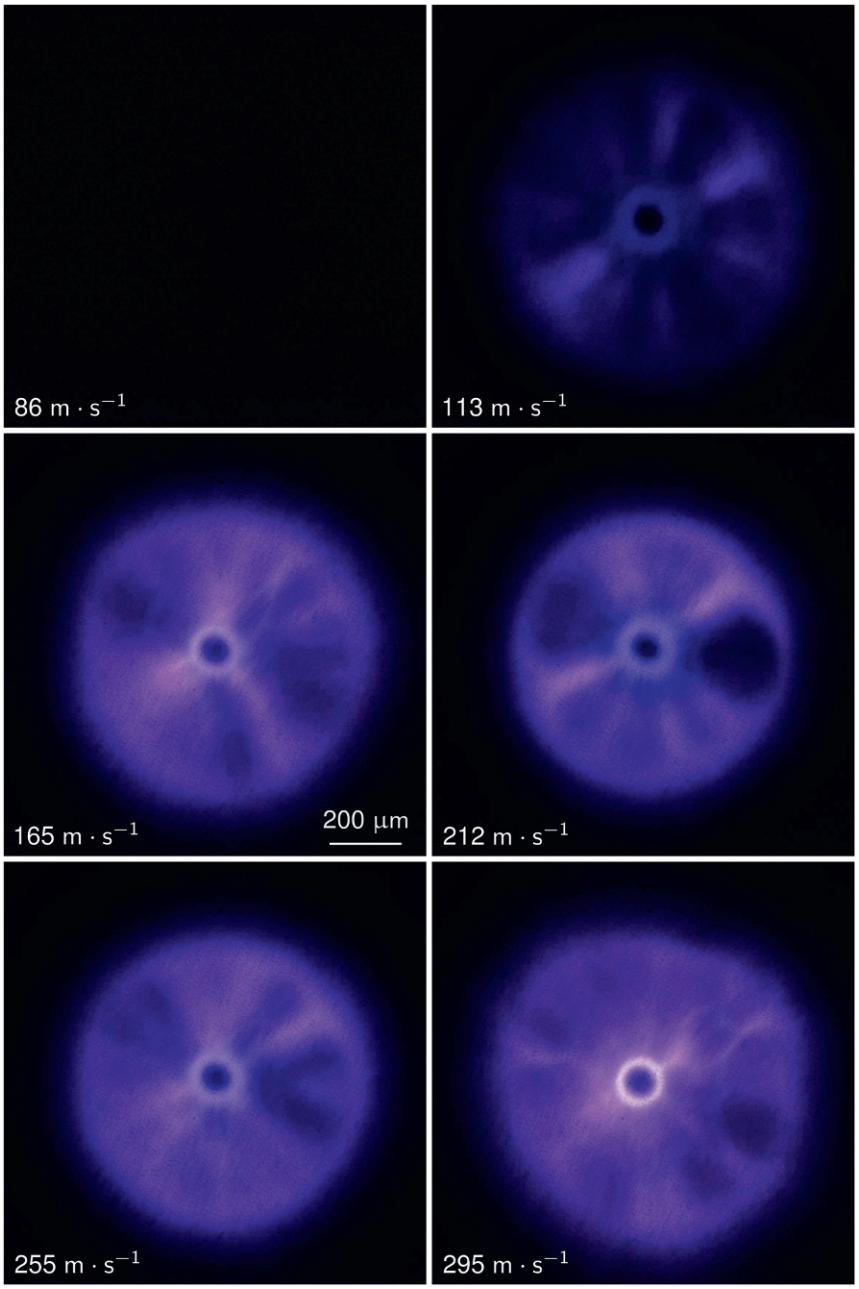

Fig. S3. Corona in air on a fine-ground lithium niobate surface. Jet velocity is varied from 86 m · s^{-1} to 295 m · s^{-1}. Photographs were taken at ISO 20,000 and a 1/60-s exposure time with a Sony A7S camera and a 10× objective lens. Color levels of images have been enhanced by 33% for better display.

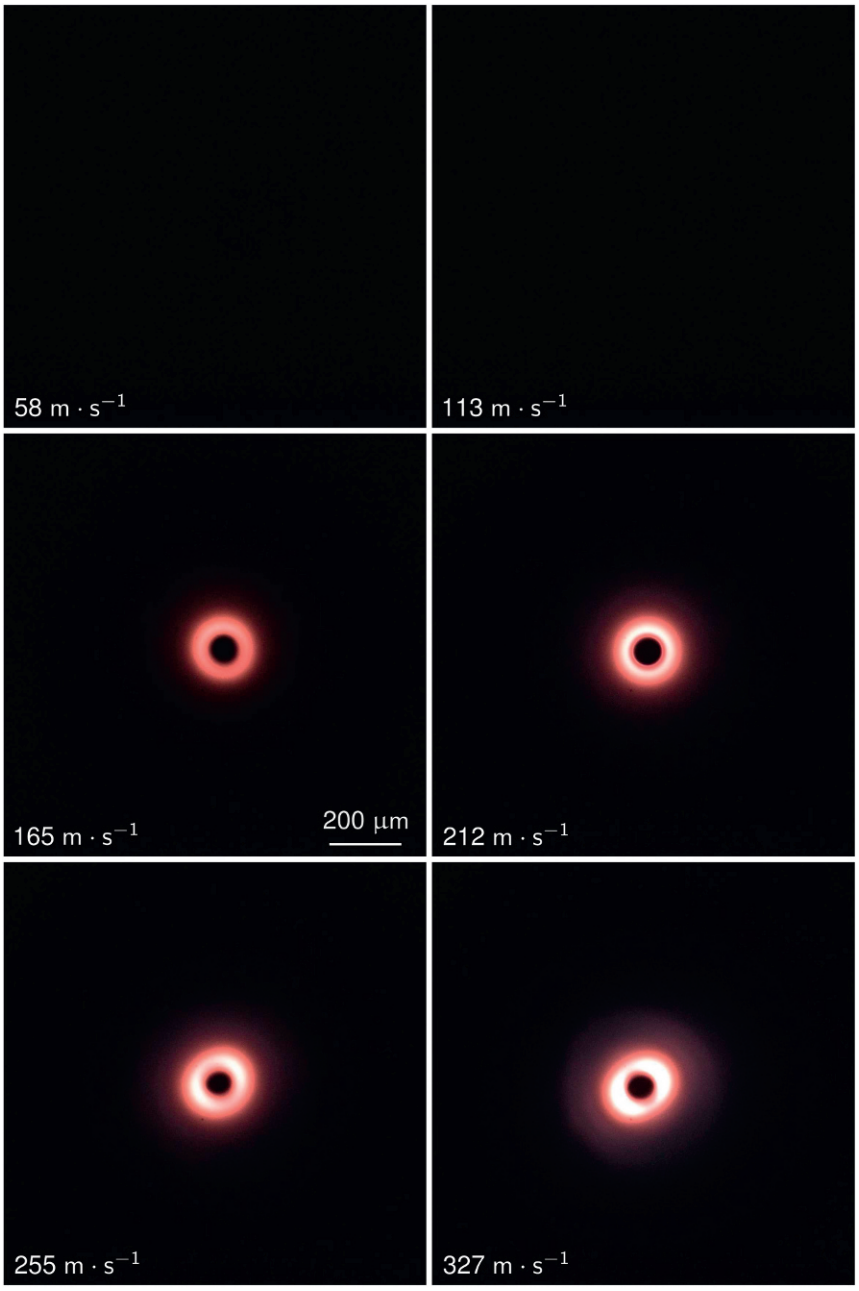

Fig. S4. Luminescence in helium on a polished quartz surface. Jet velocity is varied from 58 m · s^{-1} to 327 m · s^{-1}. Photographs were taken at ISO 12,800 and a 1/60-s exposure time with a Sony A7S camera and a 10× objective lens. Color levels of images have been enhanced by 33% for better display.

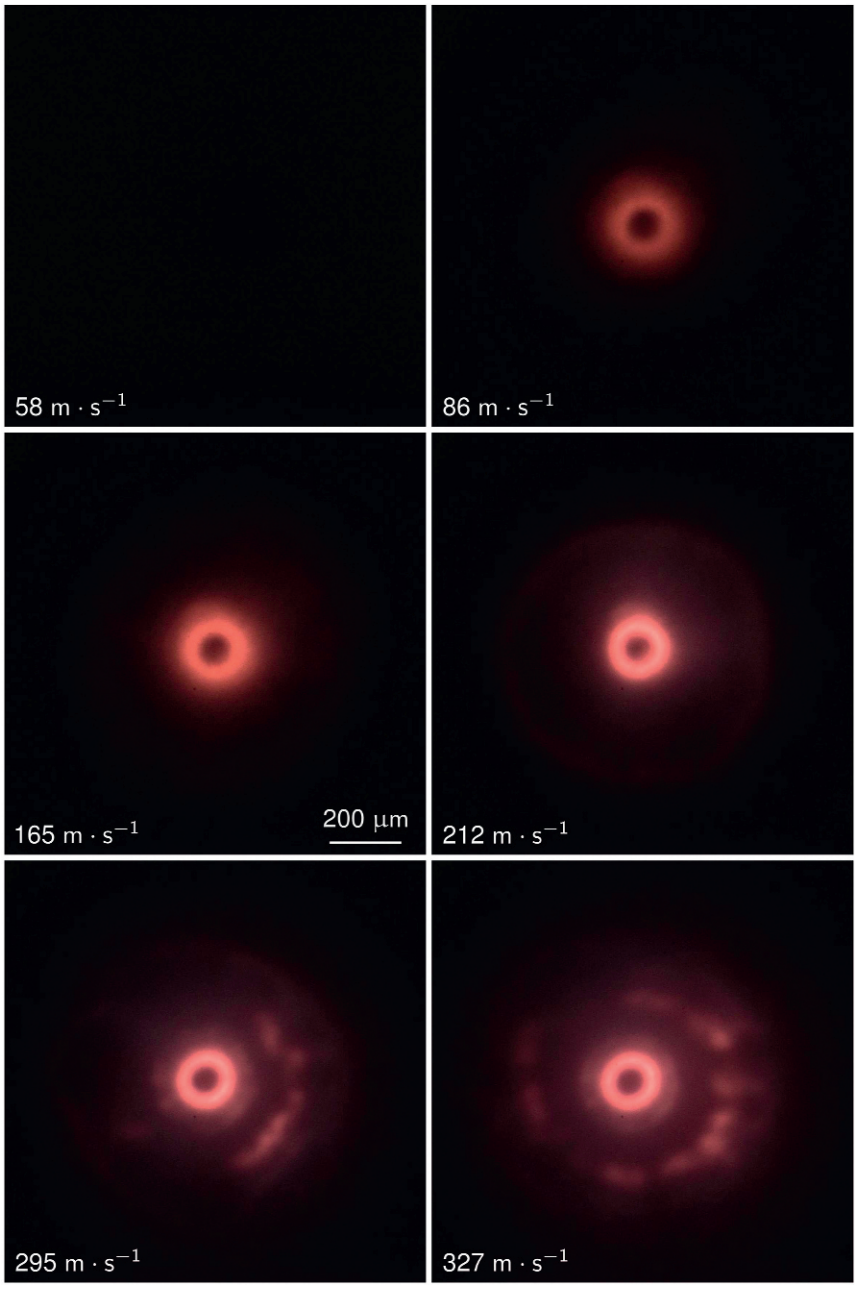

Fig. S5. Luminescence in helium on a fine-ground lithium niobate surface. Jet velocity is varied from 58 m · s^{-1} to 327 m · s^{-1}. Photographs were taken at ISO 12,800 and a 1/60-s exposure time with a Sony A7S camera and a 10× objective lens. Color levels of images have been enhanced by 33% for better display.

Fig. S6. RF antenna. The customized RF antenna is shown in its setup position relative to the jet nozzle. The antenna axis is colinear with the jet axis.

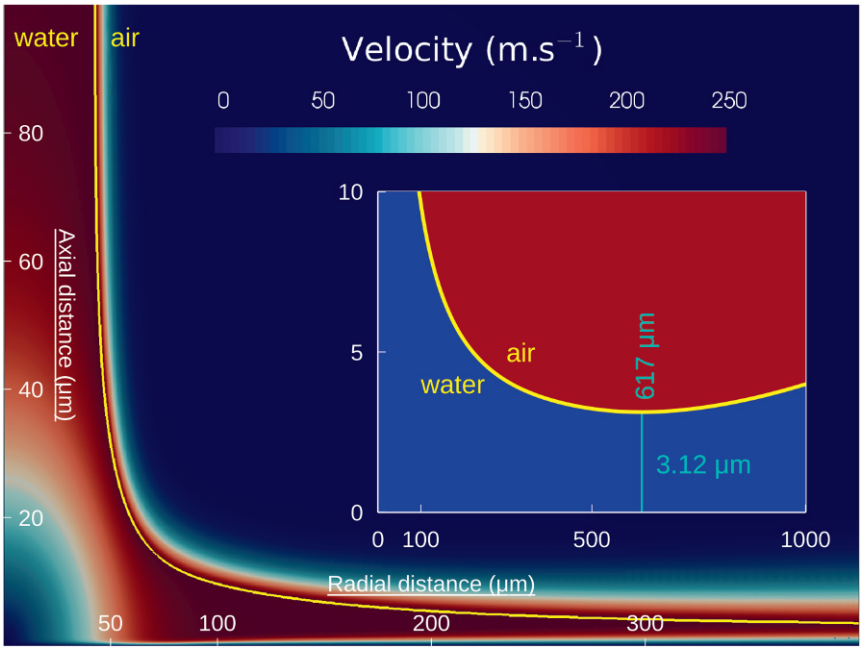

Fig. S7. Computational fluid dynamics simulation of the impinging jet flow. The 2D calculations were done for a nominal jet speed of 250 m · s^{-1}. The color plot shows the map of the velocity magnitude, with the yellow line representing the air–water interface. *Inset* outlines the thinning of the wall jet to a minimum of 3.12 μm at a radial distance of 617 μm from the jet axis. Scales of axes are in micrometers.

Table S1. Possible chemical reactions in air, in liquid water, and at the interface for the air plasma (corona) and helium plasma

Reaction identification letter	Reaction type or product	Chemical equation
In air with corona		
A)	N_2/O_2 dissociation	$N_{2(g)} + e^* \Rightarrow 2N_{(g)} + e$ $O_{2(g)} + e^* \Rightarrow 2O_{(g)} + e$
B)	Associative ionization	$N^*_{(g)} + N_{(g)} \Rightarrow N^+_{2(g)} + e$
C)	Nitric oxide	$2N_{(g)} + 2O_{(g)} \Rightarrow 2^{\bullet}NO_{(g)}$
D)	Zeldovich exchange reactions	$N_{2(g)} + O_{(g)} \Rightarrow {}^{\bullet}NO_{(g)} + N_{(g)}$ $N_{(g)} + O_{2(g)} \Rightarrow {}^{\bullet}NO_{(g)} + O_{(g)}$
E)	Nitrogen dioxide	$2^{\bullet}NO_{(g)} + O_{2(g)} \Rightarrow 2^{\bullet}NO_{2(g)}$
F)	Nitrous/nitric acids	$2^{\bullet}NO_{2(g)} + H_2O_{(l)} \Rightarrow HNO_{2(aq)} + HNO_{3(aq)}$
G)	Hydrons, nitrites, and nitrates	$HNO_{2(aq)} \Leftrightarrow H^+_{(aq)} + NO^-_{2(aq)}$ $HNO_{3(aq)} \Leftrightarrow H^+_{(aq)} + NO^-_{3(aq)}$
H)	Hydronium	$H^+_{(aq)} + H_2O_{(l)} \Leftrightarrow H_3O^+_{(aq)}$
At air–water interface with corona		
I)	Impact ionization by positive ions ($\oplus$)	$\oplus + H_2O_{(l)} \Rightarrow H_2O^*, H_2O^+{}_{(aq)} + e_{(aq)}$
J)	Dissociation	$H_2O^+{}_{(aq)} \Rightarrow {}^{\bullet}OH_{(aq)} + H^+_{(aq)}$
K)	Protonation	$H^+_{(aq)} + H_2O_{(l)} \Leftrightarrow H_3O^+_{(aq)}$
L)	Recombination	$H_3O^+_{(aq)} + e_{(aq)} \Rightarrow H_2O_{(l)} + H_{(aq)}$
M)	Diffusion	$H_{(aq)} \Rightarrow H_{(g)}$
N)	Ionization	$H_{(g)} + e^* \Rightarrow H^+_{(g)} + e^* + e$
O)	Back diffusion and hydration	$H^+_{(g)} + H_2O_{(l)} \Rightarrow H_3O^+_{(aq)}$
In liquid water		
P)	Dissociation	$H_2O_{(l)} + e^* \Rightarrow {}^{\bullet}OH_{(aq)} + {}^{\bullet}H_{(aq)} + e$ $H_2O_{(l)} + e^* \Rightarrow OH^-_{(aq)} + H^+_{(aq)} + e$
Q)	Protonation	$H^+_{(aq)} + H_2O_{(l)} \Leftrightarrow H_3O^+_{(aq)}$
R)	Self-ionization	$2H_2O_{(l)} \Leftrightarrow H_3O^+_{(aq)} + OH^-_{(aq)}$
S)	Recombination	$H_3O^+_{(aq)} + OH^-_{(aq)} \Leftrightarrow 2H_2O_{(l)}$

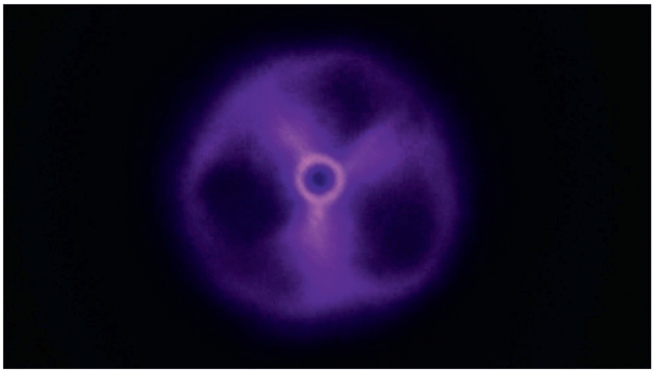

Movie S1. Luminescence in air on a rough $LiNbO_3$ surface. The movie was taken with a 10× optical magnification and shows how the luminescence pattern is affected by the surface roughness. We can observe the formation of radial streamers that bridge the central toroidal plasma with a plasma ring located approximately at 500 μm from the jet impinging site. The streamers are seen to interact collectively and to give a visual perception of rotation, resembling the streamers seen in plasma balls.

Movie S1

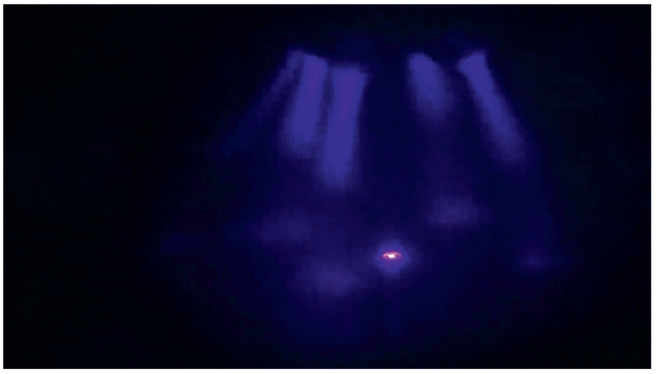

Movie S2. Effect of high electric potential on the plasma stability and viability. The movie was taken from the impinging side and shows that the application of a 50-kV potential between the wafer and the nozzle, either positive or negative, leaves the plasma structure unaffected. The luminescence was generated in a mixed atmosphere of air and helium. Secondary streamers are seen that bridge the nozzle to the wafer away from the luminescent structure at the jet impingement site. They are not connected and do not interfere with this latter phenomenon.

Movie S2